

Continuous bunch-by-bunch spectroscopic investigation of the micro-bunching instability

Johannes L. Steinmann,* Miriam Brosi, Erik Bründermann, Michele Caselle, Benjamin Kehrer, Lorenzo Rota, Patrik Schönfeldt, Marcel Schuh, Michael Siegel, Marc Weber, and Anke-Susanne Müller

Karlsruhe Institute of Technology, Karlsruhe, Germany

(Dated: November 25, 2022)

Electron accelerators and synchrotrons can be operated to provide short emission pulses due to longitudinally compressed or sub-structured electron bunches. Above a threshold current, the high charge density leads to the micro-bunching instability and the formation of sub-structures on the bunch shape. These time-varying sub-structures on bunches of picoseconds-long duration lead to bursts of coherent synchrotron radiation in the terahertz frequency range. Therefore, the spectral information in this range contains valuable information about the bunch length, shape and sub-structures. Based on the *KAPTURE* readout system, a 4-channel single-shot THz spectrometer capable of recording 500 million spectra per second and streaming readout is presented. First measurements of time-resolved spectra are compared to simulation results of the *Inovesa* Vlasov-Fokker-Planck solver. The presented results lead to a better understanding of the bursting dynamics especially above the micro-bunching instability threshold.

I. INTRODUCTION

The self-interaction of a bunch with its own electric field can lead to potential well distortion and therefore to a deformation in the longitudinal phase space [1, 2]. Above the micro-bunching instability threshold, it results in the formation of sub-structures on the longitudinal bunch profile and increased emission of coherent synchrotron radiation (CSR) at wavelengths corresponding to the size of the sub-structures [3]. The Karlsruhe Research Accelerator (KARA) is the electron storage ring of the test facility and synchrotron radiation source ANKA at the Karlsruhe Institute of Technology (KIT). In the short-bunch operation mode, this storage ring provides picoseconds-long bunches, which results in the emission of coherent radiation in the range up to a few terahertz (THz) [4].

The fast changing sub-structures emit coherently in a different spectral range over time. Observing the radiation for the circulating electron bunches in the storage ring with single-shot detectors and turn-by-turn precision gives insights to the evolution of these structures. Previous work by *Finn et al.* [5] uses spatial segregation to record different frequencies simultaneously. In their current readout setup, the power and frequency components are analyzed in the frequency domain with spatially offset diodes. In our setup, we use wire grids as broadband beam splitters and provide, in addition, continuous streaming of bunch-by-bunch, turn-by-turn, and single-shot data by the use of our in-house developed Karlsruhe Pulse Taking Ultra-fast Readout Electronics (*KAPTURE*) [6–8]. Furthermore we compare and illustrate our results by simulations.

Here we first present simulations by the *Inovesa* Vlasov-Fokker-Planck solver [9], showing the expected

spectral evolution. Then, we introduce our 4-channel spectrometer setup. Good agreement between simulations and measurements is demonstrated.

II. VLASOV-FOKKER-PLANCK SIMULATION

Simulations have been carried out with *Inovesa* v0.14, an open source parallelized Vlasov-Fokker-Planck solver developed at KIT [9] and available on Github [10]. *Inovesa* simulates the longitudinal phase space in presence of an impedance. The simulations presented in the following use the CSR impedance with shielding by parallel plates [11]. Projecting the simulated longitudinal phase space onto the time axis provides the bunch profile. From that, the form factor and subsequently the emitted coherent radiation is calculated. Note that this is the bunch's radiation due to the parallel plates' impedance, which is not identical to the radiation observed at a beamline. The calculation of the radiation measured at the beamline requires the inclusion of additional effects such as beamline apertures, which attenuate lower frequencies, and transmission properties of the used vacuum windows and mirrors. For the comparison we omitted these effects and source specific effects like edge radiation and polarization.

The parallel plates model assumes an isomagnetic ring, where the electrons travel between two infinitely long and perfectly conducting parallel plates. Consequently, also all interactions of the bunch with its emitted field in the straight sections are neglected in this model, as are the reflections from the side walls. In our simulations, we used the bending radius (5.559 m) and beam pipe height (32 mm) of KARA. All “non-static” properties, like synchrotron frequency and RF voltage, have been chosen to fit to the measurements presented in the following (see Table I).

To compare the simulations with measurements, all values like revolution time, or bunch current have been

* johannes.steinmann@kit.edu

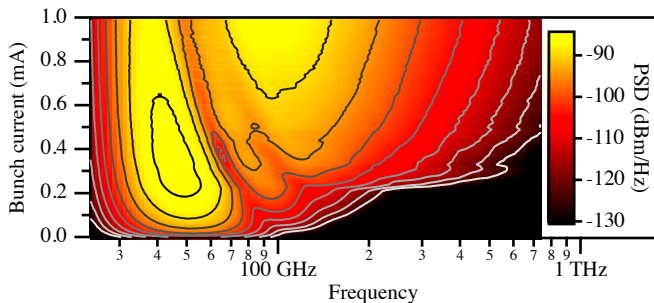


FIG. 1. *Inovesa* Simulations: Average emitted power spectral density (PSD) for different bunch currents. The contour lines are in 5 dB distance between -85 dBm and -130 dBm.

scaled to match the actual values in the existing storage ring. The simulated spectrogram in Fig. 1 shows the average emitted spectrum for different bunch currents. At zero current, the bunch is shortest and has a Gaussian shape without sub-structures. With increasing current, the bunch form changes and bunch-lengthening leads to an increase of the rms bunch length. Therefore, the intensity of the first frequency peak is decreased, even though the bunch current increases. Similarly, CSR at higher frequencies is emitted due to the non-Gaussian shape. Above the bursting threshold, additional sub-structures form and even higher frequency components arise. The threshold in this simulation is located between 0.22 mA to 0.23 mA, while the simulated current steps were 10 μ A.

This leads to an additional wake potential, which drives the instability further, and the bunch size in phase space grows. Hereafter, the emitted coherent radiation and, thus, the additional driving wake potential vanishes due to the increased bunch size. Radiation damping also smooths the bunch shape. Subsequently, the bunch shrinks according to the damping until the density threshold is reached again. In summary, the average emitted spectrum below threshold is dominated by bunch-lengthening and above threshold by the duration, intensity and repetition rate of the bursts.

Figure 2 shows in greater detail four specific spectra at 0.1 mA, 0.2 mA, 0.4 mA and 0.8 mA with an average rms bunch length of 5.0 ps, 5.2 ps, 6.7 ps and 10.9 ps, respectively.

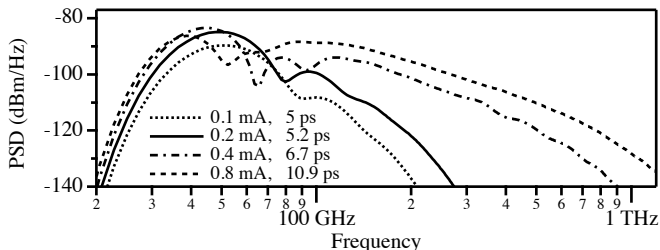


FIG. 2. *Inovesa* simulations: Slices for selected bunch currents and average rms bunch lengths of the emitted CSR spectrum in Fig. 1.

The turn-by-turn behavior and evolution of the phase space is most interesting at currents well above the bursting threshold. Figure 3 presents simulated data for a bunch current of 0.8 mA, more than three times the bursting threshold. The changing instantaneous CSR spectrum over time is calculated from the simulated bunch profiles. For comparison to slower data acquisition systems and spectrometers, the average spectrum is also displayed together with the normalized appearance of all spectra, which are emitted within 50 ms. The normalized appearance has been calculated by a histogram of every frequency bin, therefore counting the emitted intensities at every frequency over time. Then it was normalized to the number of analyzed spectra.

Most of the emitted spectra are below the average (note the logarithmic scale), because the high frequencies are emitted only for a short time during a burst. The fact that the coherent enhancement increases the emitted power by many orders of magnitude, leads to an average above the median spectrum. Also indicated are four frequency bands (Fig. 3) named like the wave guide standard in that range: WR8.0 (90 GHz to 140 GHz), WR5.1 (140 GHz to 220 GHz), WR3.4 (220 GHz to 325 GHz) and WR2.2 (325 GHz to 500 GHz). The same frequency bands are also used in the described measurements (see Table II).

Figure 3 also shows the THz intensity in the four observed spectral bands and the rms bunch length at that time. The small, but fast, bunch-length modulation between the bursts can be modelled by a dipole motion, which leads to a periodicity with twice the synchrotron frequency. On the longer timescales, the rms bunch length decreases due to radiation damping, until the threshold is reached. Then, the strong micro-bunching instability drives sub-structures and blows up the bunch. This blow-up in combination with diffusion and damping in phase space homogenizes the bunch shape and the sub-structures vanish. Accordingly, the bunch length and the energy spread fluctuation show the same periodicity as the burst behavior (see also [12]).

Three points in time (A, B and C) are shown in more detail in Fig. 4 with their spectrum and bunch profile. Time A lies between two bursts (cf. Fig. 3(d)): the shape is almost Gaussian since the sub-structures have already decayed, and the bunch is further shortening. At the high frequencies of WR2.2 and WR3.4 very low power is emitted. At time B, the shortened bunch implies an increased wake potential, which leads to bunch deformations, visible in the bunch profile (cf. Fig. 4(b), trace B) and drives the micro-bunching instability. This results in more radiation, seen first at lower frequencies (cf. Fig. 4(a)), and also increases the intensity of the wake potential. At time C, the sub-structures, now clearly visible on the bunch profile, have the highest amplitude and shortest size leading to the outburst of radiation as seen at all frequency bands. The high wake potential blows up the bunch quickly, which due to diffusion and damping becomes stable again and shrinks until the next burst

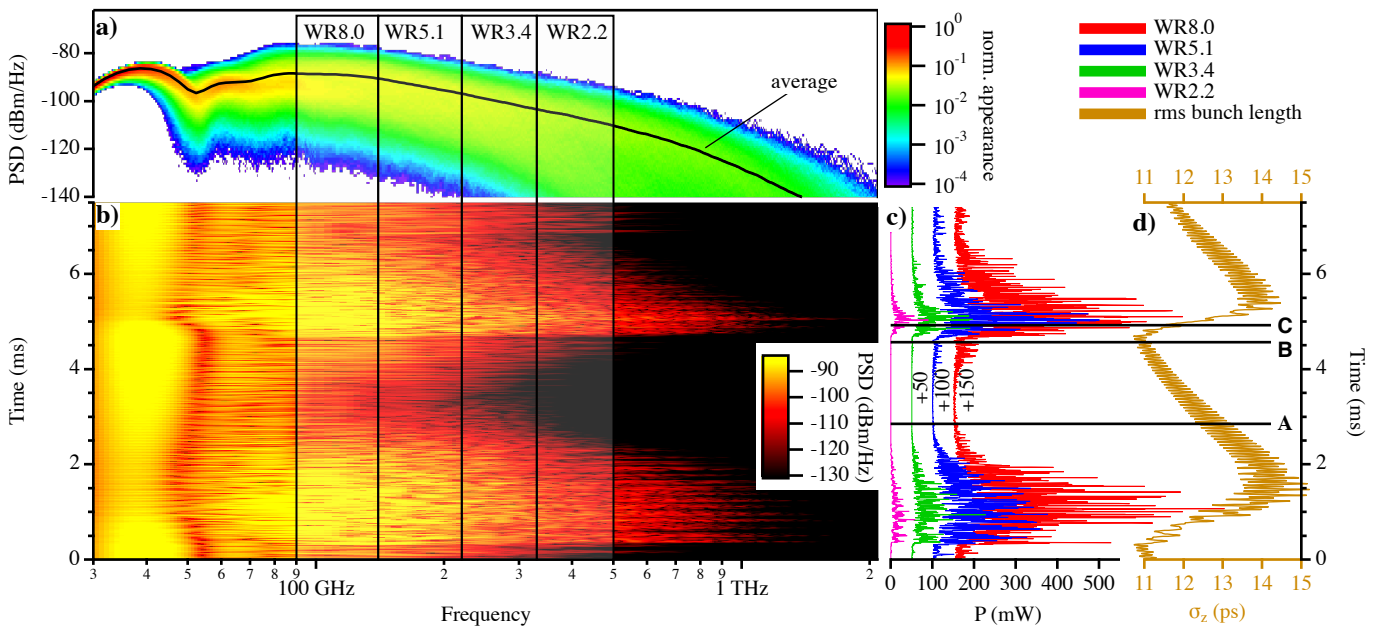


FIG. 3. *Inovesa* simulations at 0.8 mA: a) shows the average emitted spectrum on top of a histogram displaying the normalized appearance of frequency and power spectral density (PSD) values. For more information see text. The image in b) shows the instantaneous emitted coherent radiation due to the changing bunch profile over time. The expected integrated power P in the marked frequency bands of the used Schottky diodes are shown in c) and the corresponding rms bunch length σ_z in d) for the same time axis. For better visibility, the signal of the Schottky diode models WR3.4, WR5.1 and WR8 are shifted by 50 (green line), 100 (blue line) and 150 mW (red line), respectively. For selected times A, B and C see details in Fig. 4

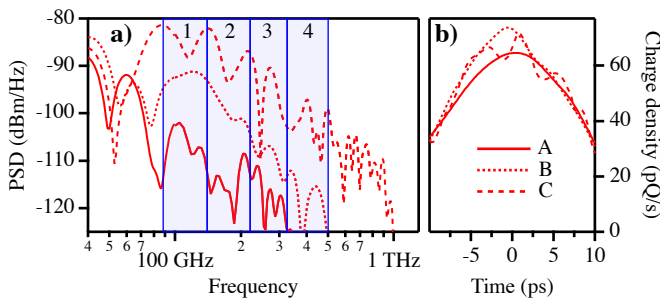


FIG. 4. Calculated emitted spectrum a) and bunch profile b) at selected times A, B and C of Fig. 3 as a function of spectral frequency and time, respectively. The high frequencies are very unstable and only emitted for a short time during a burst. However, the intensities emitted by the sub-structures are many orders of magnitude higher due to the coherent enhancement. The indicated bands 1, 2, 3 and 4 (shaded blue) correspond to the wave guide standards WR8.0 (90 GHz to 140 GHz), WR5.1 (140 GHz to 220 GHz), WR3.4 (220 GHz to 325 GHz) and WR2.2 (325 GHz to 500 GHz), respectively. For details see Fig. 3 and the text.

occurs. The described process takes a few milliseconds, only.

III. MEASUREMENT SETUP

Measurements have been performed at the storage ring KARA at KIT and the radiation was coupled to the detection system via the infrared beamline IR2 [13]. The storage ring was operated in a short-pulse mode (low-alpha operation) above the bursting threshold [4]. Important machine parameters during the measurement are summarized in Table I. By altering the magnet optics, the momentum compaction factor α_c was reduced to 5×10^{-4} . The scaling law [14] for the instability predicts, for an accelerating amplitude of 800 kV, a zero-current bunch length and threshold bunch current (“bursting threshold”) of 4.5 ps and 0.2 mA, respectively. The measurements were performed for different bunch currents between 2 mA and 0.18 mA.

The radiation was coupled out through a Z-cut quartz window at the diagnostic port of the infrared beamline. The optics of the beamline were designed to project an image of the entrance edge of the radiating bending magnet. However, the long wavelengths suffer from diffraction and limiting apertures. This was confirmed by Fourier transform infrared (FTIR) spectroscopy at the beamline measuring the maximum power around 200 GHz [16] with strong suppression of frequencies below 100 GHz.

With a set of four wire-grid polarizers the beam was first horizontally polarized and then split into four partial

TABLE I. Parameters set and calculated for the storage ring KARA

Beam energy, [15]	1.287	GeV
Circumference	110.4	m
Vacuum chamber full height	32	mm
Revolution frequency	2.7157	MHz
RF frequency	499.71	MHz
RF amplitude	799.2	kV
Synchrotron frequency	8.2	kHz
Calc. bursting threshold, [14]	0.2	mA
Calc. momentum compaction α_c	5×10^{-4}	
Calc. relative energy spread	0.47×10^{-3}	
Calc. zero-current bunch length (rms)	4.5	ps

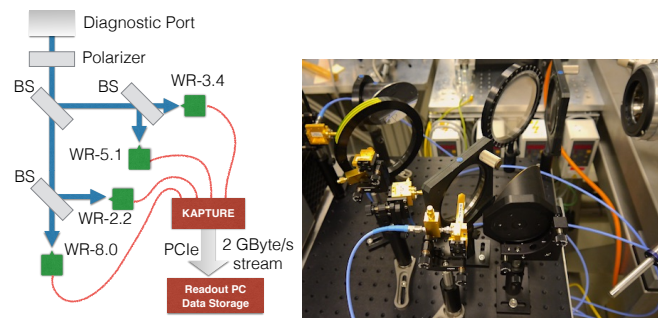


FIG. 5. The synchrotron radiation emitted at the diagnostic port is first polarized and then divided into four beams by three wire-grid beam splitters (BS). The split beams are focused onto four detectors, each one sensitive in a different frequency band (see Table II and Fig. 3 for details). The single-shot measurements are sampled and read out by the *KAPTURE* system.

beams with nearly equal power, each focused to a commercially available wave guide coupled Schottky barrier diode (SBD) detector [17] sensitive in different frequency bands (Tab. II). Each detector signal was simultaneously read out with one of *KAPTURE*'s four input channels [6–8]. The setup is sketched in Fig. 5.

KAPTURE is synchronized to the 500-MHz master clock of the storage ring and digitizes the detector signals with the same repetition rate. The sampling time can be set with a 3 ps accuracy for each input channel, individually. A track-and-hold circuit in front of the analog-to-digital converter (ADC) stores the signal amplitude at the chosen time until it is read out by the 12-bit ADC. The results presented here are based on data sets recorded in intervals of 10 seconds. Each data set consists of 100 ms continuous turn-by-turn data for all 184 RF buckets, i.e. every bunch has continuously been tracked for more than 2.7×10^5 consecutive turns.

To improve the used ADC range, three of the SBD detectors (WR5.1, WR3.4 and WR2.2) were amplified using a 15 dB amplifier with 18 GHz bandwidth. Table II lists the frequency bands and average responsivity of the used detectors.

The responsivity shown is only indicative of the sensi-

TABLE II. Schottky barrier diode detectors used [17]

VDI Model	Band (GHz)	Average DC responsivity (V/W)
WR8.0ZBD	90-140	2000
WR5.1ZBD	140-220	2000
WR3.4ZBD	220-325	1500
WR2.2ZBD	325-500	1250

tivity of the detector system, i.e. the diodes should not be compared quantitatively, because the measured synchrotron radiation pulse is broad band and the frequency acceptance of the diodes is not uniform.

Even though the analog frequency bandwidth of all diodes has been measured to be above 18 GHz, the synchrotron emits ps and sub-ps pulses shorter than the overall response time of the SBD detector circuit. Therefore, the measured pulse amplitude is dominated by the impulse response due to the quality of the RF-readout path of each individual diode. In comparison to the individual DC-responsivities, the THz impulse response is very difficult to calibrate. Thus, the data shown here was not corrected for the diode's responsivities, however, we assume that these properties do not change during the experiment. The reader has to keep in mind that quantitative comparisons between the diodes require special care.

IV. RESULTS

An important parameter to determine is the bursting threshold at the given machine settings. A good method for its determination is to measure the fluctuations of the THz signal amplitude [18]. For that reason, the standard deviation of the detector amplitude is analyzed as shown in Fig. 6. Below the threshold current, only two diodes

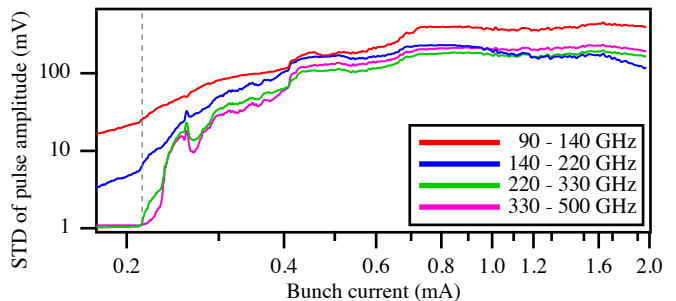


FIG. 6. Measured standard deviation (STD) of the pulse intensity in the different diode frequency bands. Above the determined bursting threshold of 0.214(2) mA (horizontal dashed line), the fluctuations increase significantly.

detect fluctuations in the pulse intensity. This is in accordance with the dipole motion model of the synchrotron oscillation that modulates the bunch length. The slope increases significantly at the threshold current, where ad-

ditional unstable sub-structures influence the emitted radiation. In the two higher frequency bands, almost no signal is observed and thus no fluctuations could be measured below the threshold.

The determined bursting threshold is at 0.214(2) mA, which is in good agreement to the threshold predicted by the scaling law (0.20(1) mA) and the one simulated by *In-ovesa* (0.225(5) mA). Uncertainties on the measured input parameters account for the error in scaling law value but have not been considered in the VFP simulation. Above the threshold, the standard deviation increases until it stays at a high level, which is even above the average amplitude. That is due to the outbursts of radiation followed by relatively low power during the shrinking of the bunch. Consequently, long averaging times are needed in this regime, if one intends to do conventional spectroscopy with typically, in comparison to our measurements, slower data acquisition systems.

So-called *bursting spectrograms* have proven to be an excellent tool to analyze the bursting dynamics. For this purpose, the time domain data of THz pulses and their time evolution is Fourier transformed. The resulting spectrum is plotted over each corresponding measured bunch current. For a more detailed description of the data analysis strategy, see [18]. Such a spectrogram, showing specific modulation frequencies of the THz power, is reproducible and depends on machine parameters like the momentum compaction factor, the accelerating voltage and the impedance of the storage ring. It is a fingerprint of the accelerator in its current state. Figure 7 shows the spectrogram for each of the four detectors. Different current-dependent bursting regimes can be identified [18].

Above the bursting threshold at 0.214(2) mA, the instabilities start with high frequency modulations around 32 kHz. With increasing current, also low frequencies arise that indicate the occurrence of regular bursts. The repetition rate of the bursts is below 1 kHz and hardly visible in the plots. After an intermediate stage with more complex structures above 0.7 mA, the spectrum changes to a regular pattern of harmonics near the synchrotron frequency. With increasing bunch current the amount of white noise also rises. Since the ADC pre-amplifier has not been changed, these are not digitization-induced fluctuation effects, but account for a high amount of randomness in the bursting behavior. As a consequence, even though the form of the bursts is similar and their appearance repeats, none of them are identical.

Furthermore, it can be seen that the main features of the spectrogram are the same, although the different diodes span different frequency ranges from 90 GHz to 500 GHz. Differences in the spectrogram can be seen in relative intensity variations of some features, the amount of white noise and the number of visible harmonic structures.

In the following, a time-domain dataset at 0.8 mA is analyzed in more detail. This current is about four times the bursting threshold and in the regime of large periodic

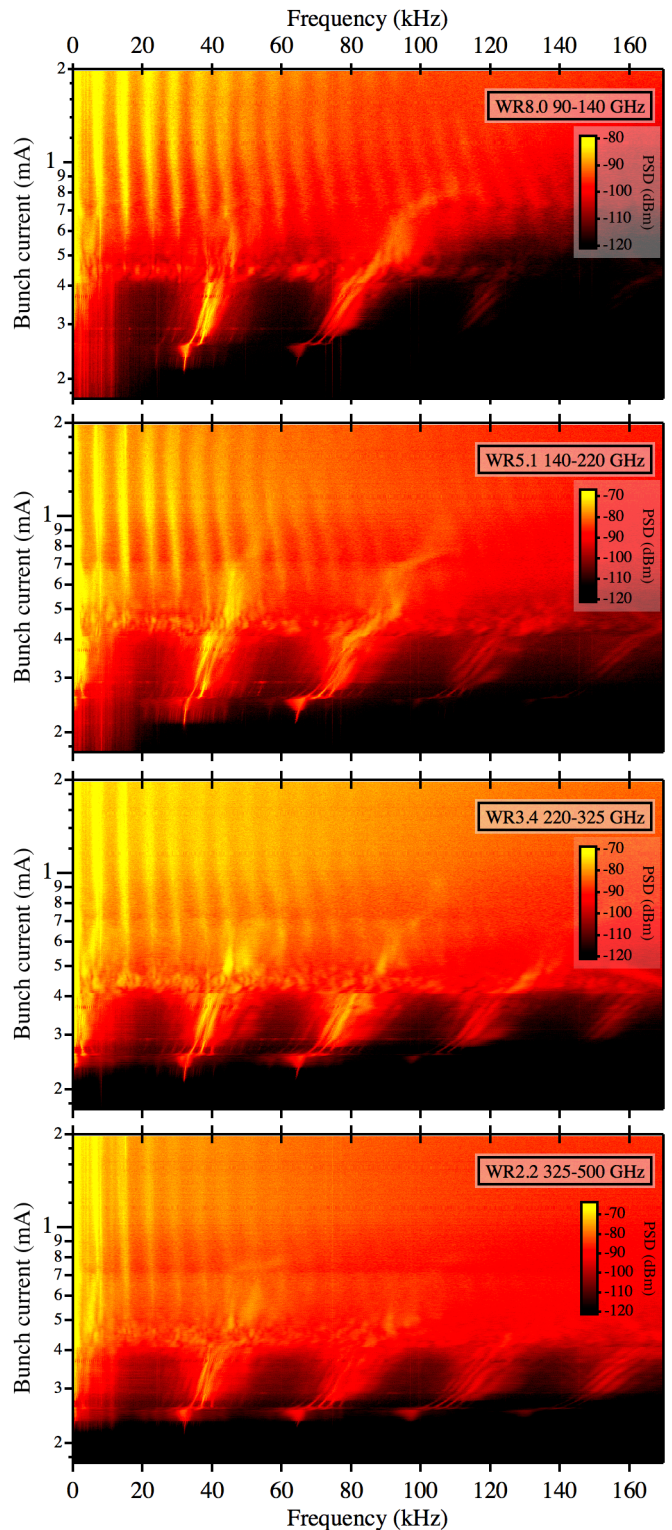


FIG. 7. Bursting spectrograms of each detector. The main features are visible in all spectrograms, albeit with different contrast. The color scale is a logarithmic dBm scale of the detector output power into 50 Ohms and should not be compared quantitatively between the diodes due to differing frequency bandwidth, responsivity and RF readout efficiency of the diodes. Also note that the WR8.0 diode was operated without amplifier, whereas all other diodes were amplified by 15 dB

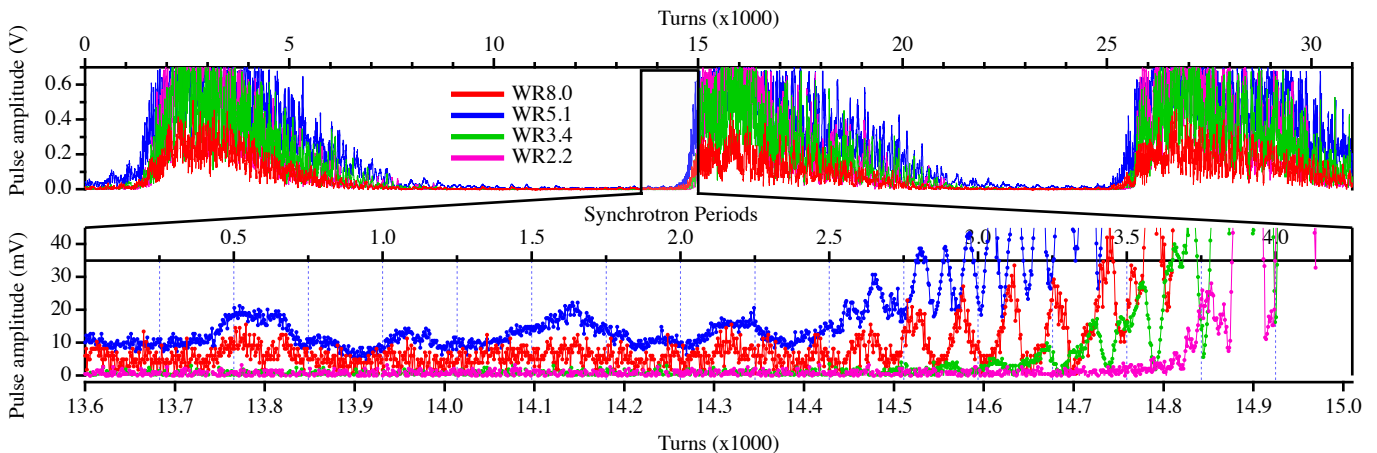


FIG. 8. Measured turn-by-turn amplitudes of the four different diodes (1000 turns \approx 0.368 ms \approx 3 synchrotron periods). The bottom panel shows a zoom-in to the beginning of a burst. Every point is a measured pulse amplitude, the connecting line is a guide to the eye.

bursts. Due to bunch lengthening, the average bunch length is rather long, which limits the amount of coherent radiation. Nevertheless, the strong instability with many small sub-structures in the electron density leads to periodic bursts of high amplitude THz radiation.

Turn-by-turn data of the four detectors are shown in Fig. 8. In agreement with the simulations (compare to Fig. 3), the pulse amplitudes of the WR8.0 and WR5.1 diodes are on an almost constant and low level before the burst. They are mainly modulated with twice the synchrotron frequency in accordance with the dipole motion model. The diodes, sensitive at a higher frequency band, do not measure notable coherent radiation until the burst starts. Additionally, the burst's observation occurs later compared to the lower frequencies bands.

Because of the uniqueness of the bursts, a direct comparison between measurement and simulation is difficult. Even though a burst may look similar in simulation and experiment, its underlying physics do not necessarily have the same origin. To cross-check both, averaged values are compared derived from our simulations with *Inovesa* and the measurements obtained with our experimental setup. The average measured amplitude is shown in Fig. 9. Note that the electrical output voltage of the SBD detector is proportional to the optical input power.

The bursting threshold can be identified slightly above 0.2 mA (Fig. 9). Noteworthy is the different behavior of the diodes' signal at this threshold value. The forming of sub-structures above the bursting threshold only has a minor effect at the WR8.0 frequency band between 90 GHz to 140 GHz. This is attributed to the already high amount of coherence from the bunch as a whole, so that the sub-structures increase mostly affects higher frequency components. The latter is evident in the data obtained in the two highest frequency bands. Without sub-structures, these diodes hardly detect any radiation while they are not sufficiently sensitive for incoherent radiation in this setup. Note that the sudden drop of de-

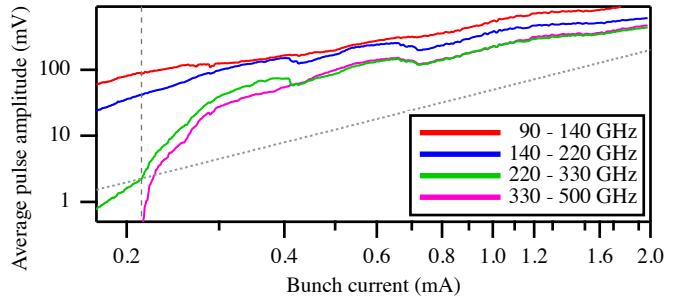


FIG. 9. Average measured amplitude of the single pulse signal over the bunch current corresponding to the average optical power emitted in each frequency band. The WR8.0 data (90 GHz to 140 GHz) was compensated to account for the missing amplifier. For a stable bunch profile, a quadratic dependency would be expected. To guide the eye, the dotted line shows such a behaviour. The bursting threshold appears at 0.214(2) mA (vertical dashed line).

tected power for the two diodes WR5.1 and WR3.4 above 0.4 mA and for all three diodes with frequency bands above 140 GHz around 0.7 mA (cf. Fig. 9) is due to a change of the bursting behavior. These sudden drops in the average values correlate with distinct features in the spectrograms (Fig. 7), i.e. these average traces are highly reproducible and sudden drops are connected to the underlying electron density dynamics.

If we assume a stable bunch shape, a quadratic increase of CSR with current is expected (see Fig. 9). This can be seen for the two lowest frequency bands, however, the bunch is not short enough for coherent radiation at the higher frequencies. Around the threshold, with the starting potential well distortion resulting in an asymmetric bunch shape and formation of substructures, the power at the higher frequencies increases stronger than linear as shown in our simulations (cf. Figs. 1 and 2).

Above the threshold, the influence of the changing form

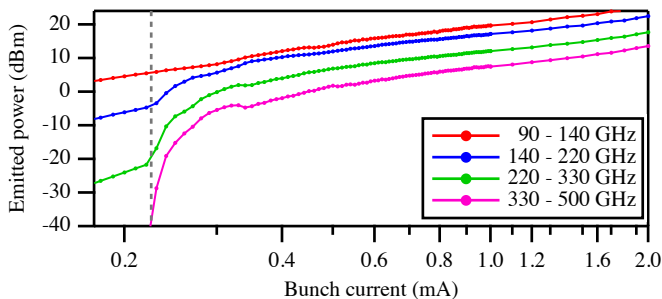


FIG. 10. *Inovesa* Simulations: Average integrated CSR power emitted in each frequency range of the measurement. The connecting line between the simulation steps is a guide to the eye. The vertical dashed line denotes the bursting threshold at 0.225(5) mA. This is the simulated power emitted by the bunch over the whole turn. For details see text.

factor due to the sub-structures is stronger than the number of the overall electrons. Subsequently, a larger power increase can be observed for a small current range at higher frequencies in comparison to the quadratic behavior (cf. Fig. 9). This saturates quickly, as the bunch can not radiate stronger than fully coherent. Above 0.7 mA, in the regime of the resonant bursts described before, the average power is determined by the length and repetition rate of the bursts.

Figure 10 shows a similar behavior for the simulated data. In agreement with the measurements, the simulated and derived averages in the low frequency WR8.0 band almost show no change at the threshold, but similar changes are visible in the higher frequency bands although the sudden drops in the experimental data (cf. Fig. 9) are less pronounced in comparison. In the simulations, the threshold is found at a slightly higher bunch current. Considering that the only impedance taken into account is the CSR impedance shielded by parallel plates, *Inovesa* mimics the measured data. In conclusion, the measured phenomena can be attributed to the micro-bunching instability and can be simulated by a Vlasov-Fokker-Planck solver.

V. SUMMARY AND OUTLOOK

In summary, we have set up a single-shot 4-channel spectrometer, which continuously streams 500 million spectra per second. The optical set-up consists of three beam splitters and four individual detectors, which are simultaneously read out in a streaming mode by the in-house build data acquisition system *KAPTURE*. Accordingly, the micro-bunching instability could be observed in four THz frequency bands turn-by-turn in a multi-bunch environment. Furthermore, the found features agree with simulations by our Vlasov-Fokker-Planck solver *Inovesa*, which opens the door to a better understanding and possible pathways to influence the bursting dynamics.

In the future, we plan to extend *Inovesa* from the basic parallel plates to an improved impedance model. The improved model can include arbitrary impedances like resistive wall losses and edge radiation with interaction in the subsequent straight sections to achieve an even better agreement between simulations and measurements. Developments are under way to use integrated single-chip detector arrays [19, 20] based on superconducting, electric field-sensitive YBCO detectors [21] and on room-temperature Schottky detectors [22] in combination with the next version of *KAPTURE*. The latter will provide eight readout channels and an improved readout path [8]. Synchronization with other experimental stations at KARA will additionally provide time-resolved information about the energy spread [12] and the longitudinal bunch profile [23–25], simultaneously [26].

ACKNOWLEDGMENTS

We would like to thank Y.-L. Mathis and his team from the IBPT Infrared Group at KIT. This work has been supported by the Initiative and Networking Fund of the Helmholtz Association under contract number VH-NG-320 and the German Federal Ministry of Education and Research (BMBF) under grant no. 05K16VKA. M. Brosi, P. Schönfeldt and J. Steinmann acknowledge the support of the Helmholtz International Research School for Teratronics (HIRST) and E. Blomley the support of the Karlsruhe School of Elementary Particle and Astroparticle Physics (KSETA).

-
- [1] M. Venturini, R. Warnock, R. Ruth, and J. A. Ellison, *Phys. Rev. ST Accel. Beams* **8**, 014202 (2005), URL <https://link.aps.org/doi/10.1103/PhysRevSTAB.8.014202>.
- [2] G. Stupakov and S. Heifets, *Phys. Rev. ST Accel. Beams* **5**, 054402 (2002), URL <https://link.aps.org/doi/10.1103/PhysRevSTAB.5.054402>.
- [3] M. Abo-Bakr, J. Feikes, K. Holdack, P. Kuske, W. B. Peatman, U. Schade, G. Wüstefeld, and H.-W. Hübers, *Phys. Rev. Lett.* **90**, 094801 (2003), URL <https://link.aps.org/doi/10.1103/PhysRevLett.90.094801>.

- [aps.org/doi/10.1103/PhysRevLett.90.094801](https://doi.org/10.1103/PhysRevLett.90.094801).
- [4] A.-S. Müller, A. Hofmann, N. Hiller, E. Huttel, K. Il'in, V. Judin, B. Kehrer, M. Klein, S. Marsching, C. Meuter, S. Naknaimueang, et al., in *ICFA Beam Dynamic Newsletter* (2012), vol. 57.
- [5] A. Finn, P. Karataev, and G. Rehm, *Journal of Physics: Conference Series* **732**, 012039 (2016), URL <http://stacks.iop.org/1742-6596/732/i=1/a=012039>.
- [6] M. Caselle, M. Brosi, S. Chilingaryan, T. Dritschler, V. Judin, A. Kopmann, A.-S. Mueller, J. Raasch, N. J.

- Smale, J. Steinmann, et al., in *2014 19th IEEE-NPSS Real Time Conference* (2014), pp. 1–3, URL <https://dx.doi.org/10.1109/RTC.2014.7097535>.
- [7] M. Caselle, M. Balzer, S. Chilingaryan, M. Hofherr, V. Judin, A. Kopmann, N. J. Smale, P. Thoma, S. Wuensch, A.-S. Müller, et al., *Journal of Instrumentation* **9**, C01024 (2014), URL <http://stacks.iop.org/1748-0221/9/i=01/a=C01024>.
- [8] M. Caselle, L. A. Perez, M. Balzer, A. Kopmann, L. Rota, M. Weber, M. Brosi, J. Steinmann, E. Bründermann, and A.-S. Müller, *Journal of Instrumentation* **12**, C01040 (2017), URL <http://stacks.iop.org/1748-0221/12/i=01/a=C01040>.
- [9] P. Schönfeldt, M. Brosi, M. Schwarz, J. L. Steinmann, and A.-S. Müller, *Phys. Rev. Accel. Beams* **20**, 030704 (2017), URL <http://link.aps.org/doi/10.1103/PhysRevAccelBeams.20.030704>.
- [10] P. Schönfeldt, *Inovesa source code*, URL <https://github.com/Inovesa/Inovesa>.
- [11] R. L. Warnock, in *4th Advanced ICFA Beam Dynamics Workshop on Collective Effects in Short Bunches* (1990), SLAC-PUB-5375, p. 10, URL <https://cds.cern.ch/record/215286>.
- [12] B. Kehrer, E. Blomley, M. Brosi, E. Bründermann, N. Hiller, A.-S. Müller, M. Nasse, M. Schedler, M. Schuh, M. Schwarz, et al., in *Proc. of International Particle Accelerator Conference (IPAC'17), Copenhagen, Denmark, 14-19 May* (2017), pp. 53–56, URL <http://jacow.org/ipac2017/papers/moocb1.pdf>.
- [13] Y.-L. Mathis, B. Gasharova, and D. Moss, *Journal of Biological Physics* **29**, 313 (2003), ISSN 0092-0606, URL <http://dx.doi.org/10.1023/A%3A1024429801191>.
- [14] K. L. F. Bane, Y. Cai, and G. Stupakov, *Phys. Rev. ST Accel. Beams* **13**, 104402 (2010), URL <https://link.aps.org/doi/10.1103/PhysRevSTAB.13.104402>.
- [15] C. Chang, E. Bründermann, E. Hertle, N. Hiller, E. Huttel, A.-S. Müller, M. Nasse, M. Schuh, J. L. Steinmann, H.-W. Hübers, et al., in *Proceedings of the 6th International Particle Accelerator Conference (IPAC'15)* (2015), URL <http://jacow.org/IPAC2015/papers/mopha040.pdf>.
- [16] Steinmann, J.L. and Hertle, E. and Hiller, N. and Judin, V. and Müller, A.-S. and Schuh, M. and Schönfeldt, P. and Schütze, P. and Bründermann, E., in *Proceedings, 5th International Particle Accelerator Conference (IPAC'14)* (2014), URL <http://jacow.org/IPAC2014/papers/thpme124.pdf>.
- [17] *Virginia Diodes, Inc., Charlottesville, VA*, URL <http://vadiodes.com>.
- [18] M. Brosi, J. L. Steinmann, E. Blomley, E. Bründermann, M. Caselle, N. Hiller, B. Kehrer, Y.-L. Mathis, M. J. Nasse, L. Rota, et al., *Phys. Rev. Accel. Beams* **19**, 110701 (2016), URL <http://link.aps.org/doi/10.1103/PhysRevAccelBeams.19.110701>.
- [19] A. Schmid, J. Raasch, A. Kuzmin, J. Steinmann, S. Wuensch, M. Arndt, M. Siegel, A.-S. Müller, G. Cinque, and M. Frogley, *IEEE Transactions on Applied Superconductivity* **27**, 1 (2017), ISSN 1051-8223, URL <https://dx.doi.org/10.1109/TASC.2016.2625763>.
- [20] A. Schmid, M. Brosi, E. Bründermann, K. Ilin, B. Kehrer, K. Kuzmin, A.-S. Müller, J. Raasch, M. Schuh, P. Schönfeldt, et al., in *Proceedings, 7th International Particle Accelerator Conference (IPAC'16)* (2016), URL <http://jacow.org/ipac2016/papers/mopmb016.pdf>.
- [21] J. Raasch, A. Kuzmin, P. Thoma, K. Ilin, M. Arndt, S. Wuensch, M. Siegel, J. Steinmann, A.-S. Müller, E. Roussel, et al., *IEEE Transactions on Applied Superconductivity* **25** (2015), URL <https://doi.org/10.1109/TASC.2014.2365138>.
- [22] M. Schiselski, M. Laabs, N. Neumann, S. Kovalev, B. Green, M. Gensch, and D. Plettemeier, in *2016 IEEE MTT-S International Microwave Symposium (IMS)* (2016), pp. 1–4, URL <https://dx.doi.org/10.1109/MWSYM.2016.7540173>.
- [23] N. Hiller, A. Borysenko, E. Hertle, V. Judin, B. Kehrer, S. Marsching, A.-S. Müller, M. Nasse, M. Schuh, P. Schönfeldt, et al., in *Proceedings, 5th International Particle Accelerator Conference (IPAC'14)* (2014), URL <http://jacow.org/IPAC2014/papers/weobb02.pdf>.
- [24] P. Schönfeldt, E. Blomley, E. Bründermann, M. Caselle, S. Funkner, N. Hiller, B. Kehrer, A.-S. Müller, M. Nasse, G. Niehues, et al., in *Proc. of International Particle Accelerator Conference (IPAC'17)* (2017), pp. 227–230, URL <http://jacow.org/ipac2017/papers/mopab055.pdf>.
- [25] N. Hiller, Ph.D. thesis, Karlsruhe Institute of Technology (2013), karlsruhe, KIT, Diss., 2013, URL <http://digbib.ubka.uni-karlsruhe.de/volltexte/1000041159>.
- [26] B. Kehrer, M. Brosi, J. L. Steinmann, E. Blomley, E. Bründermann, M. Caselle, S. Funkner, N. Hiller, M. J. Nasse, G. Niehues, et al. (2017), arXiv:1709.08973, submitted to PRAB.